Integration of Time-Series Interferometric Synthetic Aperture Radar Imagery and LiDAR Point Cloud for Monitoring and Analysis of Liquefied Natural Gas Storage Tank Exteriors

Ming Guo,[1,2] Yaxuan Wei,[1] Zhaorui Chen,[1,3] Youshan Zhao,[4,5*]
Xingyu Tang, [1]Kecai Guo,[6] and Kun Tang[4,5]

[1]School of Geomatics and Urban Spatial Informatics, Beijing University of Civil Engineering and Architecture,
Beijing 102616, China
[2]Key Laboratory of Modern Urban Surveying and Mapping, National Administration of Surveying,
Beijing 100044, China
[3]Lingnan University, Hong Kong 999077, China
[4]China Academy of Building Research, Beijing 100013, China
[5]CABR Testing Center Co., Ltd., Beijing 100013, China
[6]Beijing Shenxin Reach Technology Co., Ltd, Beijing 102444, China

Evaluating the integrity of liquefied natural gas (LNG) storage tanks is essential for safety and environmental conservation. In this study, which centered on an LNG storage tank on a specific island, we utilized 37 interferometric wide (IW) swath mode VV polarization Sentinel-1 images from the European Space Agency (August 2020–December 2023). Deformation data were obtained using persistent scatterer synthetic aperture radar (SAR) interferometry (PS-InSAR) and small-baseline subset SAR interferometry (SBAS-InSAR) techniques, supplemented by dense point cloud data for 3D and 2D analyses. Results showed consistent deformation rates in the tank, with peaks between October 2021 and August 2022. Point cloud analysis revealed millimeter-level localized deformations (0.1 to 2.6 mm), corroborating InSAR findings. This underscores the importance of PS-InSAR, SBAS-InSAR, and point cloud modeling in monitoring LNG tank deformations, and offers insights into managing the impact of climate change on LNG storage stability.

1.   Introduction

The integrity of liquefied natural gas (LNG) storage tanks is vital for safety and environmental protection, necessitating structural and functional soundness throughout their life cycle to ensure stability and to prevent incidents such as gas stratification or pressure issues. Regular integrity assessments are crucial.[1] Research in this sector often focuses on insulation performance, using finite element simulations and theoretical approaches, as seen in studies by

---

Enpal[2] and Oh *et al*.[3] However, most research is limited to thermal analysis, and a comprehensive approach considering environmental, chemical, seismic, and internal factors is needed for a complete understanding of LNG tanks in complex environments.

For integrity checks of LNG tank exteriors, ground subsidence and deformation are key considerations. Synthetic aperture radar (SAR), with its all-weather, high-resolution capabilities,[4–6] and persistent scatterer SAR interferometry (PS-InSAR) technology, as used by Ferretti *et al*.[7] for time-series analysis, are essential for monitoring structural subsidence and deformation. InSAR is advantageous for wide-area, precise, and continuous monitoring, unaffected by weather.[8–10] InSAR technology is applied across various fields, such as monitoring urban area subsidence,[11–13] including volcanic regions,[14] forested areas,[15] and landslide-prone zones.[16] Additionally, InSAR plays a significant role in monitoring building subsidence and is also utilized for structural deformation monitoring.[17,18] When compared with leveling measurement methods for building surveillance, both InSAR and leveling measurement methods exhibit high correlation.[19] Owing to its time-series characteristics, InSAR is particularly effective in identifying seasonal patterns or other temporal trends.[20] Terrestrial laser scanning (TLS) is also used for deformation detection but faces limitations such as ground obstacles and workload. Airborne LiDAR overcomes these limitations, offering large-scale 3D data collection, with unmanned systems reducing costs and enhancing efficiency.[20–23] This technology is applied in various fields, but its use in the drone-based monitoring of LNG tank subsidence is still limited.

2. Materials and Methods

2.1 Regional overview

The research area shown in Fig. 1 includes a natural gas storage facility on an island city in a coastal region covering around 394 square kilometers with various topographies such as hilly

Fig. 1. (Color online) Study area map.

and plain terraces, river valleys, and coastal plains. Nearby, the island city contains significant geological reserves, including kaolin, quartz sand, and ceramic soil. By 2020, the region's primary minerals were of low value and nonmetallic, often in contiguous, shallow formations. Understanding this complex geographical and geological context is crucial for evaluating environmental effects on the natural gas storage tanks' integrity and functionality.

2.2   Data sources

2.2.1   InSAR data

The satellite data employed in this study was acquired from the Sentinel-1A satellite, as available on the Alaska Satellite Facility (ASF) official website. The Sentinel satellite system, a collaborative endeavor between the European Space Agency (ESA) and the European Commission (EC), was developed and operationalized for various applications commencing in October 2014. This system comprises two satellites, Sentinel-1A and Sentinel-1B, with Sentinel-1A functioning on a 12-day global imaging revisit cycle. The data source for PS-InSAR originates from a time frame between August 2020 and December 2023, with a total of 37 SAR scenes. The details of these images are found in Fig. 2.

2.2.2   DEM data

The digital elevation model (DEM) is a digital simulation of the terrain using elevation data. DEM is an essential spatial information resource in the geographic information system (GIS)
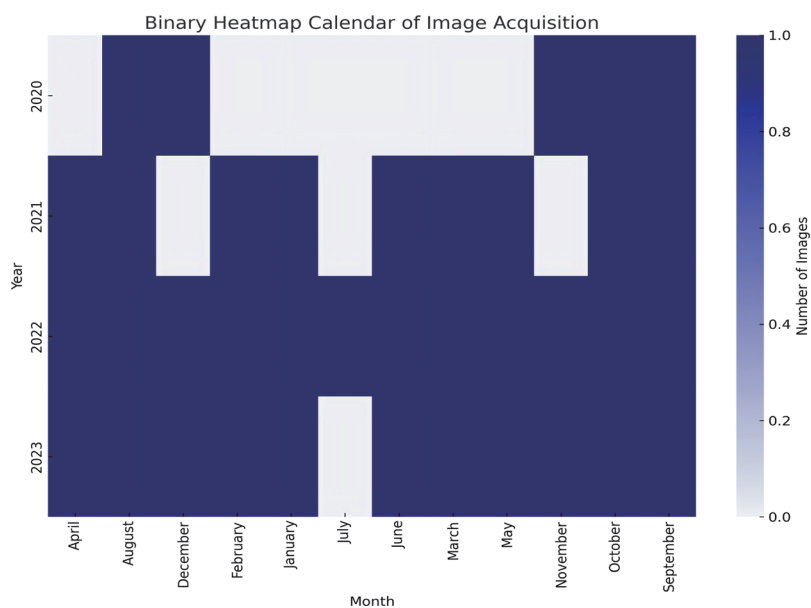

Fig. 2.   (Color online) Binary heatmap calendar of image acquisition.

database, and it is also the core data system for terrain analysis. National surveying and mapping departments regard DEM as one of the important components of the construction of the national spatial data infrastructure. The DEM data used in this paper were downloaded from the Shuttle Radar Topography Mission (SRTM) Tile Grabber, which consists of four TIFF files corresponding to the study area, as shown in Fig. 3. The files were stitched together using the seamless mosaic module and exported in the software format.

2.2.3 Point cloud data

The experiment employed the airborne LiDAR-derived point cloud data collected in May 2023, covering four LNG tanks in a specific island area. The surveyed zone, totaling approximately 0.096 square kilometers, included extensive platform surfaces of these tanks. Flight parameters included a velocity of 14 m/s, an altitude of 110 m, and a lateral overlap above 70%. Figure 4(a) shows the resultant airborne laser point cloud. Additionally, over 2000 drone images from two periods were obtained through drone imagery. After processing these images, dense point cloud data were generated, as shown in Figs. 4(b) and 4(c).
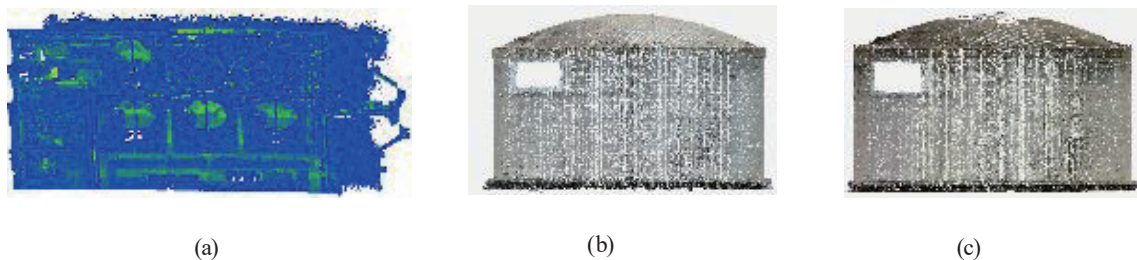

Fig. 3.   DEM data.

(a)	(b)	(c)

Fig. 4.   (Color online) (a) Airborne radar point cloud data, (b) first-phase dense point cloud data, and (c) second-phase dense point cloud data.

2.3 Methodology

The technical route is shown in Fig. 5. In this study, we employed PS-InSAR and small-baseline subset SAR interferometry (SBAS-InSAR) techniques for monitoring the subsidence and deformation of an LNG storage tank and its surrounding environment on a specific island. Given the suitability of PS-InSAR results for areas with numerous buildings, further analysis of these results was conducted. PS points were registered with Google satellite imagery to achieve precise spatial alignment, facilitating the cross-validation of selected deformation points on the tank. A 3D point cloud model of the tank area was generated using airborne LiDAR data, onto which Google satellite imagery was superimposed, enhancing the visual accuracy of the model in representing the actual terrain and facilitating comparison with PS-InSAR deformation results. Dense point cloud models derived from drone imagery were used for 2D and 3D comparative analyses to study localized deformations of the tank and evaluate these against the PS-InSAR findings.

2.3.1 Persistent scatterer interferometric SAR measurement technology

The core idea of PS-InSAR is to select points that have stable reflections and persist over time [known as persistent scatterers (PSs)] from a series of radar images. Through the long-term
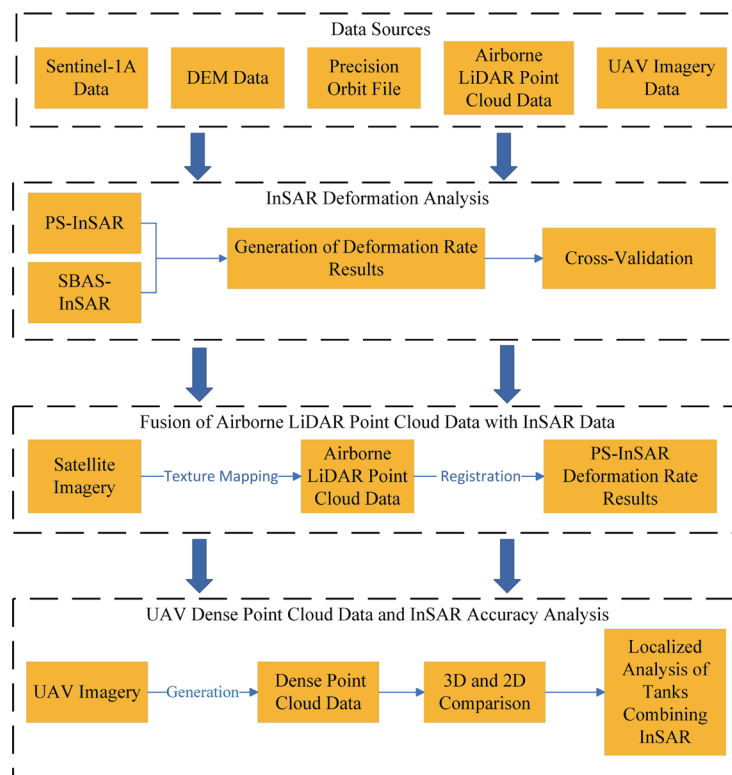

Fig. 5.   (Color online) Technical route.

sequential analysis of these targets, more accurate ground deformation information can be obtained. Among the existing $N + 1$ SAR images, one is automatically selected as the master image, and the rest are used as slave images.[24] All slave images are matched with the master image to obtain N sets of interferograms. To eliminate the effect of terrain, differential interferometry is performed on all interferogram pairs using known external DEM data, and the amplitude dispersion index (D) is estimated on the basis of the processing results. The D value in $N + 1$ SAR images is

$$D = \frac{\mu}{\sigma}, \tag{1}$$

where μ is the amplitude mean of the pixel in all images and σ is the amplitude standard deviation of a pixel over time.

In an image sequence, when the amplitude information of a pixel is consistent or nearly identical across the images, the phase deviation of that pixel will be relatively small. During the interferometric processing, there is no need to analyze the phase, as the potential coherent points can be identified by calculating the D value, which is faster, and there is still much unknown information in the interferometric phase of the pixels. The PS points within the SAR image can be obtained through the calculated D value. To conduct accurate analysis, the stability of the PS points must meet certain criteria (variation of less than 1 mm), and then the information of these stable PS points is analyzed and calculated. The phase value calculation formula of the interferometric image is

$$\Phi = \varphi_{mov} + \varphi_{top} + \varphi_{orb} + \varphi_{atm} + \varphi_{noi}. \tag{2}$$

In this equation, Φ represents the phase of the PS point in the interferogram, φ_{mov} represents the deformation phase along the line of sight, φ_{top} represents the residual topographic phase, φ_{orb} represents the residual orbital phase, φ_{atm} represents the atmospheric phase, and φ_{noi} represents the noise phase, which includes temporal decorrelation noise, spatial decorrelation noise, system noise, and other noises.

The initial step involves using a linear model to create an interferogram from the original SAR images. This model estimates the deformation rate and residual elevation information using data from all available differential interferograms. Calculations are focused on pixels exhibiting high coherence. This includes the deformation rate and elevation correction value, but this result has not yet removed the phase affected by the atmosphere.

The linear model for the first inversion of PS is expressed as

$$DISP = V \times (t - t_0). \tag{3}$$

In this equation, $DISP$ represents the deformation quantity at time t and V represents the deformation rate. Using the products of the first inversion, we further estimate the target elevation and the deformation rate in the line-of-sight direction, and also estimate and remove

the atmospheric information in the differential interferogram to generate the final deformation result.

Owing to the significant atmospheric effect in coastal areas, atmospheric correction data are more necessary for inland areas where such an effect might be less pronounced. The removal of atmospheric filtering is mainly achieved through high-pass filtering in time and low-pass filtering in space. The purpose of the second inversion is to remove the phase error related to the atmosphere and obtain the final deformation rate. The linear model for the second inversion of PS is expressed as

$$DISP = K + V \times (t - t_0),\qquad(4)$$

where *DISP* represents the deformation at time *t*, *K* is a constant (used for fitting), and *V* is the deformation rate. All the processed results are projected from the SAR coordinate system to the geographic coordinate system for easier observation, analysis, and mapping [Fig. 6(a)].

A good PS candidate must be sufficiently stable, including common features in urban residential areas such as tank tops and bridges, as well as other man-made buildings such as houses, dams, and metal and concrete characteristic objects. In addition to artificial features, natural features such as rocks can also serve as PS candidates. From the distribution map of PS points, it can be seen that the PS points are densely distributed at the platform and port connection of the LNG tank, and only a very small number of PS points are distributed in the surrounding area of the platform and port path. Because there are no obvious landmarks in the surrounding area of the platform and port path, the instability of the scatterers in the resolution unit at the moment of radar imaging leads to severe incoherence problems, such as a decrease in coherence, which leads to a decrease in the number of PS points, as shown in Fig. 6(b).

2.3.2 Differential interferometry short baseline subset

The availability of *N* + 1 SAR images arranged in a time series is assumed. The SBAS-InSAR technique pairs the images based on preset time and space thresholds, resulting in numerous small sets. The interferometric baselines within these small sets are relatively short, whereas those between sets are relatively long. The final number of interferograms obtained will
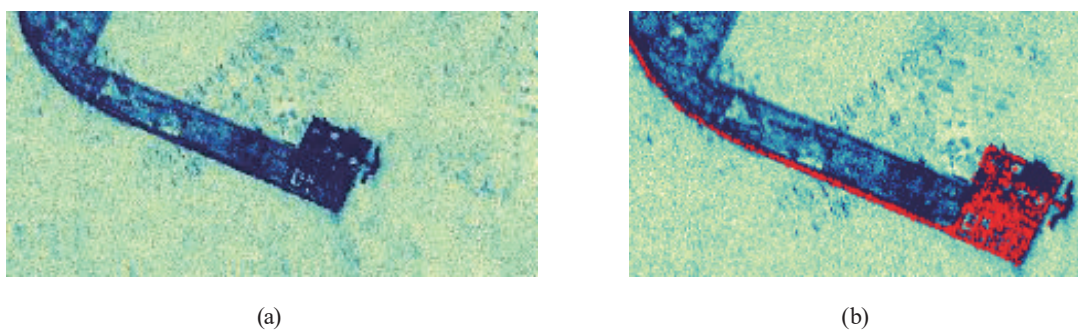

(a) (b)

Fig. 6. (Color online) (a) Mean_geo average intensity image and (b) PS results.

fall within a range of *L*. To fully understand the SBAS-InSAR technique and its utility in interferometry, detailed explanations of how it operates and its specific applications are essential.

$$\frac{N+1}{2} \ll L \ll \frac{N(N+1)}{2} \tag{5}$$

$\varphi(b_m, x, y)$ of any given pixel (x, y) at both the initial time and a subsequent time can be determined, and all differential interference phases can be expressed as $(x, y) = (l = 1, ..., L)$. By differential interference processing on a pair of images taken at times *i* and *j*, a differential interference image can be obtained as follows.

$$\delta\varphi_1(x,y) = \varphi(b_i,x,y) - \varphi(b_j,x,y) = \frac{4\Pi}{\lambda}\left(\varphi(b_i,x,y) - \varphi(b_j,x,y)\right) \tag{6}$$

After differential interferometric processing on a pair of images at two moments, *i* and *j*, one can obtain their differential interferogram. By removing the flat earth effect and the topographic phase, the interferometric phase of any point within the interferogram can be expressed through a formula. The formula does not yet introduce phase changes due to the terrain and atmosphere for ease of understanding and calculation. According to the above formula, with L differential interferograms, L equations can be listed and replaced in matrix form.

$$\hat{\varphi}(x,y) = \left(A^T A\right)^{-1} A^T \varphi(x,y) \tag{7}$$

In the equation, *A* is an approximate correlation matrix, and the estimated value can be obtained by the least squares method.

For the above formula, if $L > 1$, then $A^T A$ is a singular matrix with a rank of $N - L + 1$. The coefficient matrix is rank deficient, and the equation group will have infinitely many solutions. To obtain a unique solution, many baseline sets should be merged to perform the singular solution decomposition method. Finally, the least squares solution with the smallest norm is obtained, which can calculate the deformation rate in the study area, as shown in Fig. 7. The deformation rate is integrated over time to obtain the cumulative subsidence during the observation period.
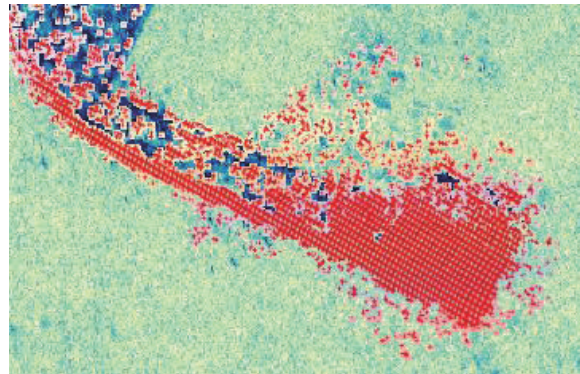

Fig. 7.　(Color online) SBAS results.

2.3.3   Satellite and airborne data integration

Image registration methods are divided into relative and absolute registrations. Relative registration selects one image as a reference from multiple images, aligning others to any coordinate system. Absolute registration establishes a control grid, aligning all images to it through individual geometric corrections to a common coordinate system. Aligning PS data with image maps allows the intuitive observation of point data locations, aiding further analysis. In this study, we focus on the relative registration of large-scale, multiple images, emphasizing the mapping relationship among them. The least squares polynomial fitting method typically facilitates translation, rotation, and affine transformations between images. This approach transforms the image registration process into one of identifying polynomial coefficients, ultimately guiding the decision-making process. Six parameters are identified for transforming grid rows and columns to map coordinates. In this experiment, orthoimages from Google Maps are registered with SAR images by applying the least squares polynomial fitting technique and a feature-point-based registration method to rotate and translate corresponding points, as demonstrated in Fig. 8.

The feature-point-based image registration method aligns two images using predetermined feature points extracted from both reference and source images. These points, characterized by unique geometric or structural attributes such as corners or edges, are resilient to noise and outliers. The corresponding feature points in the image pairs are denoted as $P = \{p_1, p_2, p_3, ..., p_n\}$ and $Q = \{q_1, q_2, q_3, ..., q_n\}$. These matched points establish a correspondence relationship for calculating the transformation needed to align the images. Selected homonymous points for registration include distinct features such as tank partition edges and platform breakpoints. A total of seven control points were chosen, resulting in a final total registration error (RMS) of 0.000167695 m, as detailed in Table 1.

We employed airborne LiDAR to collect data from four LNG tanks on a specific island, covering a platform surface area of approximately 0.096 square kilometers. The initial extensive

Fig. 8.   (Color online) Registration of Google Map orthoimages with SAR images.

Table 1
Registration accuracy.

Number	X Source	Y Source	X Map	Y Map	Residual_x	Residual_y	Residual
1	**0.13565149	**0.38369423	**0.13544923	**0.38400356	0.00004400	−0.00006834	0.00008128
2	**0.14130271	**0.38127908	**0.14051748	**0.38205240	0.00002705	0.00004159	0.00004961
3	**0.13371882	**0.38019446	**0.13385499	**0.38085078	−0.00013085	0.00003579	0.00013565
4	**0.11128079	**0.38957386	**0.11362809	**0.38871489	−0.00017521	−0.00018295	0.00025332
5	**0.13156494	**0.37642134	**0.13247342	**0.37722210	0.00007884	−0.00007970	0.00011210
6	**0.13746027	**0.37398526	**0.13765374	**0.37525333	−0.00003954	000002528	0.00004592
7	**0.11377243	**0.38800973	**0.11628539	**0.38766857	0.00019572	0.00022834	0.00030074

point cloud data required preprocessing to eliminate redundant points that could lead to modeling errors and computational burdens. Essential preprocessing steps included denoising and filtering to remove outlier points and reduce errors, as shown in Fig. 9.

Data encapsulation refers to the process of converting massive points into triangles to approximate and restore the CAD entity model, transforming the point stage into the polygon stage. Owing to the factors inherent to the model, such as occlusion, damage, and geometric topology, holes and gaps would be produced after encapsulation. These could be filled using the hole filling function in the software. Subsequently, the filled rough model was smoothed and polished to obtain the final LNG tank point cloud model. In subsequent processing, texture mapping is applied to the encapsulated point cloud model using the Google satellite imagery shown in Fig. 10(a), making the model more closely resemble the actual scene [Fig. 10(b)].

Since the deformation rate results of PS-InSAR are in geodetic coordinates, they can be matched with the geodetic coordinates of airborne radar. As shown in Fig. 10(c), which is the effect after matching, the PS points of the tank in the middle of the second row are mainly distributed in the southwest direction of the tank.

3. Results

3.1 InSAR deformation analysis results

To accurately compare InSAR results, we juxtaposed the deformation rates of LNG tanks on a specific island using both the PS-InSAR and SBAS-InSAR techniques. Deformation rate maps were generated using each technique, revealing both similarities and differences. The annual deformation rates from both techniques showed basic consistency in trends. The PS-InSAR results indicated general stability or a slight uplift around the tanks, with annual average subsidence rates ranging from −3.2 to 3.7 mm/y and cumulative subsidence between −14.4 and 15.2 mm/y. SBAS-InSAR yielded rates between −3.5 and 4.2 mm/y, with cumulative subsidence from −13.5 to 17.3 mm/y, showing close agreement. Both techniques indicated overall stability with localized uplifts near platforms and harbors.

The time series analysis of homonymous points in subsiding and stable areas showed high consistency. About 95% of PS points (PS-InSAR) and 91% of coherent points (SBAS-InSAR) within the LNG tank area had deformation rates within 3 and 4 mm/y, respectively. The difference in the number of coherent points within 1 mm/y may arise from the different
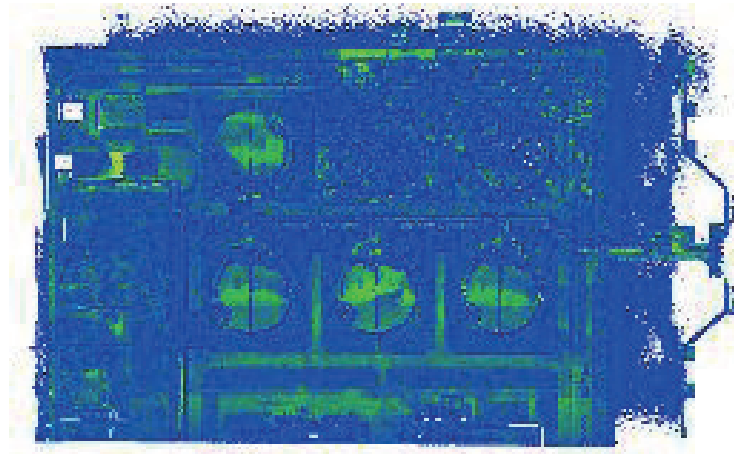
Fig. 9.   (Color online) Preprocessed point cloud data.

(a)   (b)   (c)
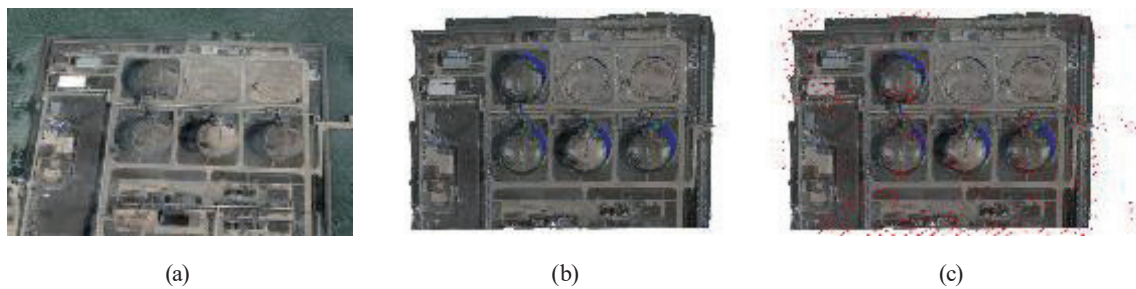
Fig. 10.   (Color online) (a) Google satellite imagery and (b) after texture mapping the point cloud model. (c) Fusion of point cloud model and PS points.

processing methods and threshold settings considered. Despite interpolation in later stages, manual selection and software extraction can introduce errors, contributing to discrepancies. For a more precise comparison, Tank 2 in the island area was selected for detailed analysis using both the PS-InSAR and SBAS-InSAR results (Fig. 11).

The results of analysis show that both the PS-InSAR and SBAS-InSAR techniques detect the maximum subsidence around August, with SBAS-InSAR indicating a slight uplift near the tank. In terms of deformation rate distribution, PS-InSAR encompasses about 73% of the area within −2.5 to 2 mm/y, whereas SBAS-InSAR covers roughly 45% within −3.5 to 3 mm/y. This suggests a general consistency between the two temporal analysis methods, despite notable differences in area proportions within the −2.5 to 2 mm/y range. However, these disparities do not significantly impact the accuracy of deformation monitoring owing to overall deformation stability. To facilitate subsequent analysis, nine PS points were selected, and their data locations on the tank are shown in Fig. 12.

The deformation information of nine pixel points was selected, which are the results of PS-InSAR and SBAS-InSAR. Since some points are not available in SBAS-InSAR, interpolation was performed on the results of SBAS-InSAR, and the deformation information line chart of each point is shown in Fig. 13.

Planar deformation rate diagram of LNG storage tank in a region
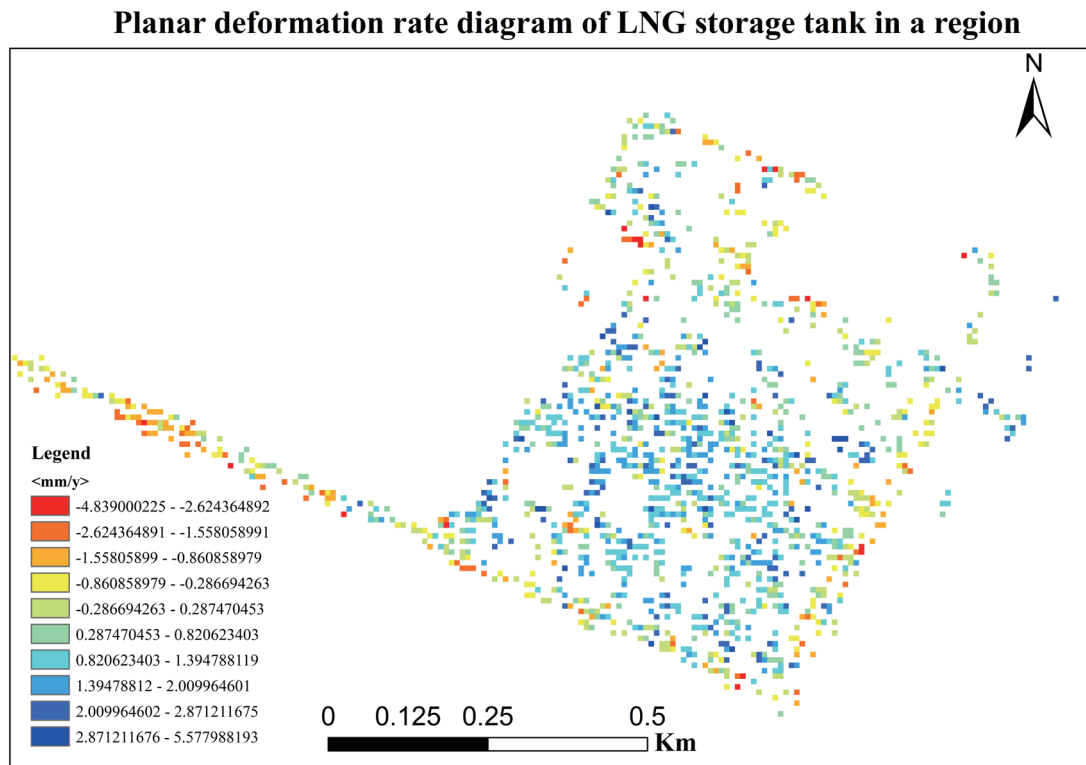

Fig. 11.   (Color online) Planar deformation rate diagram of LNG storage tank in region.
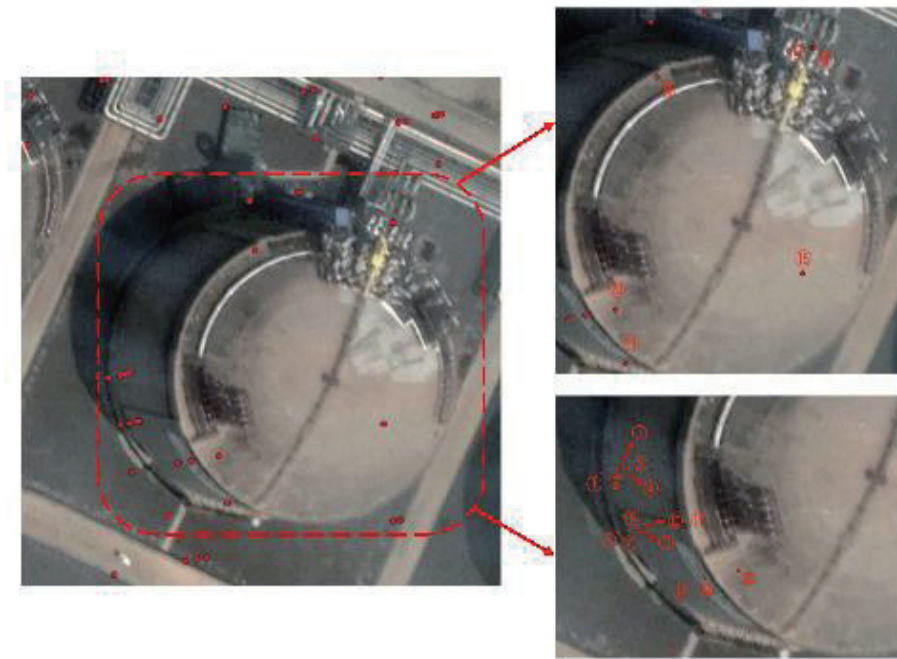

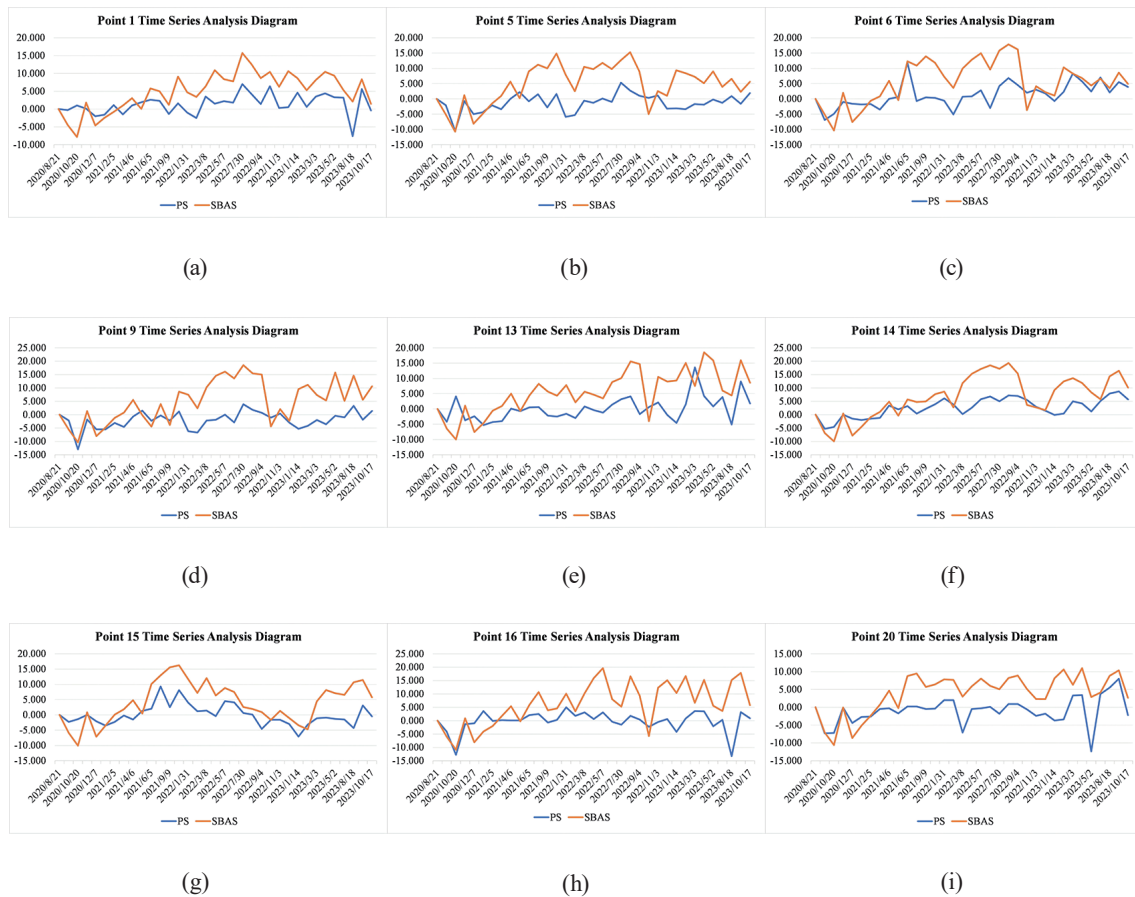Fig. 12.   (Color online) The PS points are located at the position of Tank 2.

Fig. 13.   (Color online) Time series analysis diagrams: (a) Point 1, (b) Point 5, (c) Point 6, (d) Point 9, (e) Point 13, (f) Point 14, (g) Point 15, (h) Point 16, and (i) Point 20.

Most of the points are located on the upper part of the tank body. After experimental analysis, it was found that the peak values of this type of point were concentrated between October 2021 and August 2022. Data from October 2021 showed that the weather was primarily cloudy, accounting for 48.4% of the month, thunderstorms 6.5%, heavy rain 4.8%, moderate rain 3.2%, showers 6.5%, light rain 14.5%, and overcast 11.3%; in August 2022, the weather situation comprised thunderstorms 33.9%, cloudy 33.9%, heavy rain 12.9%, moderate rain 4.8%, showers 12.9%, and light rain 1.6%. It can be speculated that the main reason for the settlement of the LNG tank is strongly related to the climate.

Figure 13 shows the annual average deformation of each point. We can find that whether or not it is on the tank body, the entire deformation is between −2 and 2 mm/y, as shown in Fig. 14.

This indicates that the deformation of LNG Tank 2 in the island area is related to climate and precipitation changes, rather than violent deformation under extreme conditions.
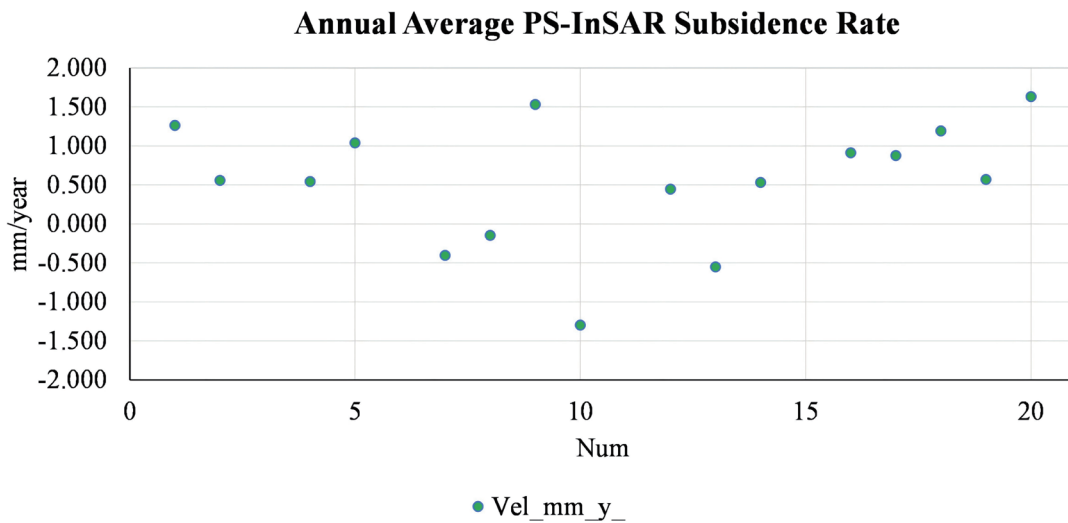
Annual Average PS-InSAR Subsidence Rate

Fig. 14.   (Color online) Annual settlement rate map of PS points.

3.2   Integrative assessment of structural changes in LNG storage tanks using combined InSAR and UAV point cloud data

To further analyze the accuracy of the InSAR results, the dense point cloud data generated from drone imagery were used for 2D and 3D comparisons on Tank 2. Since point cloud data are usually affected by measurement noise, leading to reduced data quality and errors in the modeling process, denoising and filtering were applied to the point cloud data, eliminating outliers in the study area. The denoised point clouds from two periods were encapsulated. For each point in the aligned point clouds, its distance from the corresponding point in the reference model was compared, generating a color-coded difference map that shows the deviation between the scan data and the reference model. This method only represents the overall change of the model. After the 3D comparison, the maximum deviation was toward to be 2.46 mm and the minimum deviation was found to be −4.51 mm. The deformations of the tank's front [Fig. 15(a)] and rear views [Fig. 15(b)] are uneven. The left view [Fig. 15(c)] shows the southwest direction of the tank and the right view [Fig. 15(d)] the southeast direction of the tank, with significant differences between the two. The deformation of the tank in the southwest direction is mainly a decrease, whereas in the southeast direction, it is an increase. Since the PS-InSAR results are mainly distributed in the southwest direction, the deformation in this direction was the focus of this study [Fig. 15(c)]. For a comprehensive analysis of the tank, the top, middle, and bottom parts of the tank were selected for 2D comparison.

The 2D comparative analysis involves projecting the point cloud data onto a 2D plane to generate 2D contours or slices, which are then compared with those of the reference model to assess the deformation of the tank. As shown in Fig. 16, at the top of the tank [Fig. 16(a)], the deformation in the southwest direction ranges from −0.3 to −0.2 mm. In the middle of the tank [Fig. 16(b)], the deformation ranges from −0.3 to −0.1 mm, and at the bottom of the tank [Fig. 16(c)], it ranges from −0.3 to −0.1 mm.
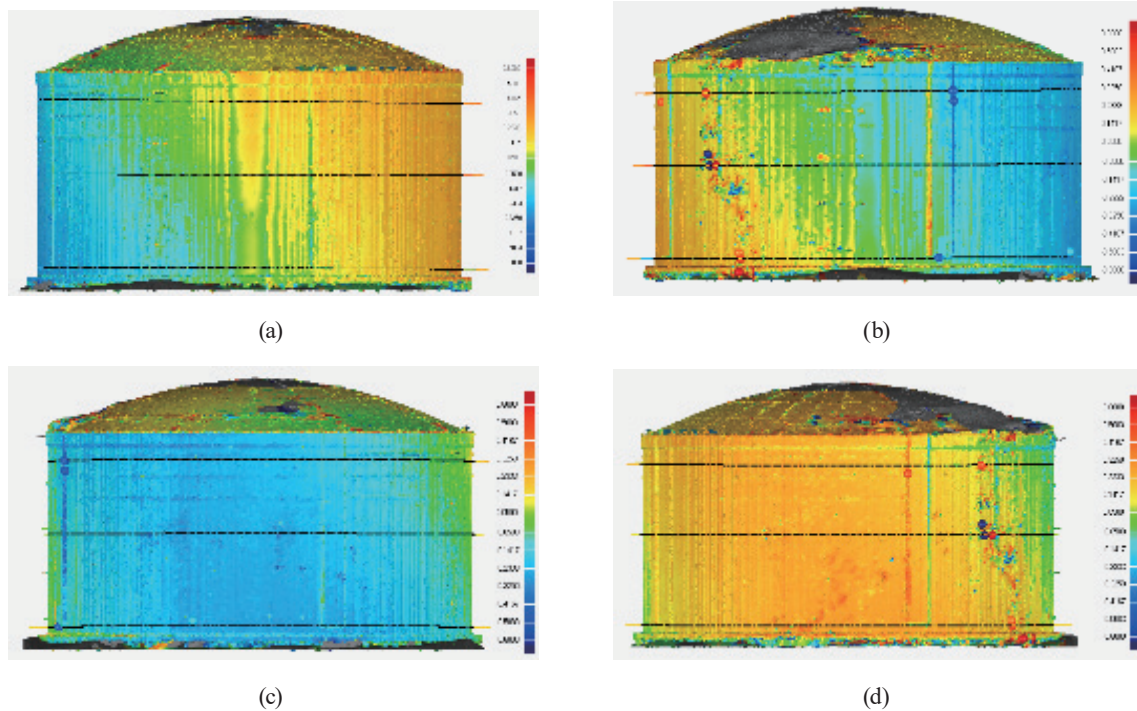
Fig. 15.   (Color online) (a) Front, (b) rear, (c) left, and (e) right views of Tank 2.
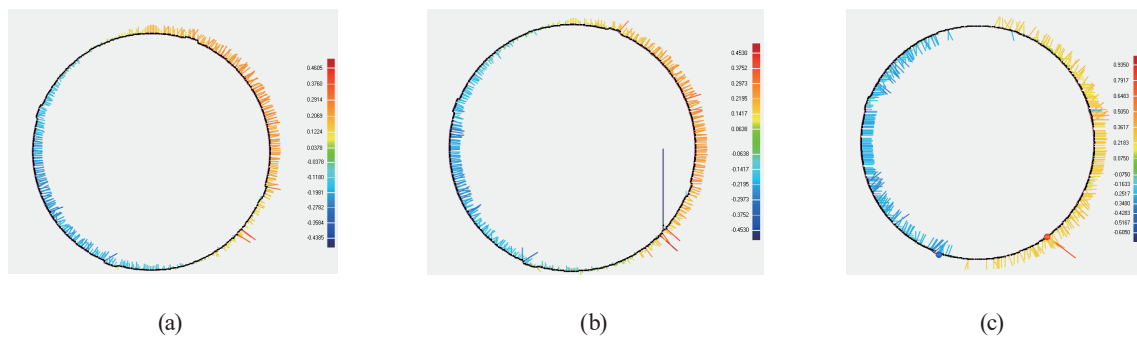

Fig. 16.   (Color online) (a) Upper, (b) middle, and (c) bottom parts of Tank 2's outer wall.

In the settlement results of the PS points, Points 1 and 6 are located at the bottom of the tank, with deformation rates of 1.2 and 2.3 mm/y, respectively. Points 5, 9, 13, and 14 are located in the middle of the tank, with deformation rates of 0.5, 0.5, 1, and 2.2 mm/y, respectively. Points 15, 16, and 20 are at the top of the tank, with deformation rates of −0.4, −0.1, and 1.5 mm/y, respectively. The deformation rates obtained from both techniques are in the millimeter range, indicating that the overall deformation rate of the tank is relatively low. This suggests that the tank structure remained relatively stable during the observation period. In particular, the negative deformation rate (i.e., slight downward trend) at the top of the tank may indicate that this part of the structure has some capacity to recover after being subjected to stress.

4.   Conclusions

In this study, we selected an LNG tank and its surroundings on a specific island as the research area, utilizing the 37 IW mode VV polarization Sentinel-1 images released by the European Space Agency from August 2020 to December 2023. Subsequently, deformation data within the study area were acquired using both the SBAS-InSAR and PS-InSAR techniques. The findings revealed consistency between the PS-InSAR and SBAS-InSAR results in terms of tank deformation rates, with peaks occurring between October 2021 and August 2022. This indicates that the deformation and subsidence of the tank in the island region are related to climatic and precipitation changes, rather than severe deformations under extreme conditions. Comparative 3D and 2D analyses using dense point clouds revealed localized deformations of the LNG tank, which were corroborated with InSAR results, showing millimeter-level deformations with differences ranging from 0.1 to 2.6 mm. In this research, we demonstrated the significant application of the PS-InSAR and SBAS-InSAR techniques, along with point cloud modeling, in monitoring deformations of LNG tanks. We also provided new insights and strategies for understanding and addressing the impact of climate change on the stability of LNG storage facilities.

Acknowledgments

References

1 C. Gas: Oil & Gas Storage and Transport (2012) 113806375. https://api.semanticscholar.org/CorpusID:113806375
2 C. Enpal: Eng. Environ. Sci. Mater. Sci. **2009** (2009) 123450173. https://api.semanticscholar.org/CorpusID:123450173
3 D.-J. Oh, J.-M. Lee, B.-J. Noh, W.-S. Kim, R. Ando, T. Matsumoto, and M.-H. Kim: Proc. Inst. Mech. Eng., Part C: J. Mech. Eng. Sci. **229** (2015) 1300. https://doi.org/10.1177/0954406215569255
4 X. Ding, Y. Chen, Z. Li, D. Zheng, and G. Liu: Adv. Earth Sci. **15** (2000) 734. https://api.semanticscholar.org/CorpusID:125740545
5 P. Zhang, X. Qian, S. Guo, B. Wang, J. Xia, and X. H. Zheng: Remote Sens. **15** (2023) 3298. https://doi.org/10.3390/rs15133298
6 A. Budillon, M. Crosetto, A. C. Johnsy, O. Monserrat, V. Krishnakumar, and G. Schirinzi: Remote Sens. **10** (2018) 1986. https://doi.org/10.3390/rs10121986
7 A. Ferretti, C. Prati, and F. Rocca: IGARSS 2000. IEEE 2000 Int. Geosci. Remote Sens. Symp. (IEEE, 2000) 761–763. https://doi.org/10.1109/IGARSS.2000.861695
8 X. Chen, V. Achilli, M. Fabris, A. Menin, M. Monego, G. Tessari, and M. Floris: Remote Sens. **13** (2021) 452. https://doi.org/10.3390/rs13030452
9 A. H.-M. Ng, Z. Liu, Z. Du, H. Huang, H. Wang, and L. Ge: Remote Sens. Environ. **295** (2023) 113694. https://doi.org/10.1016/j.rse.2023.113694

10　M. Guo, Y. Zhou, T. Zhou, and D. Pan: ISPRS - Int. Arch. Photogramm. Remote Sens. Spatial Inf. Sci., XLIII-B2-2020 (2020) 1455–1463. https://doi.org/10.5194/isprs-archives-XLIII-B2-2020-1455-2020

11　H. Sun, H. Peng, M. Zeng, S. Wang, and Y. Pan: Remote Sens. **15** (2023) 2424. https://doi.org/10.3390/rs15092424

12　G. Bonaldo, A. Caprino, F. Lorenzoni, and F. Daporto: Remote Sens. **15** (2023) 1177. https://doi.org/10.3390/rs15051177

13　F. Cigna and D. Tapete: Remote Sens. Environ. **253** (2021) 112161. https://doi.org/10.1016/j.rse.2020.112161

14　K. Spaans and A. Hooper: J. Geophys. Res.: Solid Earth **121** (2016) 2947. https://doi.org/10.1002/2015JB012752

15　H. Balzter: Prog. Phys. Geogr.: Earth Environ. **25** (2001) 159. https://doi.org/10.1177/030913330102500201

16　K. Dai, C. Chen, X. Shi, M. Wu, and W. Feng: Int. J. Appl. Earth Obs. Geoinf. **116** (2023) 103157. https://doi.org/10.1016/j.jag.2022.103157

17　W. Wu, H. Cui, J. Hu, and L. Yao: Appl. Sci. **9** (2019) 3818. https://doi.org/10.3390/app9183818

18　U. Stilla, U. Soergel, and U. Thoennessen: ISPRS J. Photogramm. Remote Sens. **58** (2003) 113. https://doi.org/10.1016/S0924-2716(03)00021-2

19　K. Yang, L. Yan, G. Huang, C. Chen, and Z. Wu: Sensors **16** (2016) 2182. https://doi.org/10.3390/s16122182

20　X. Zhang, H. Zhang, C. Wang, Y. Tang, and B. Zhang: Remote Sens. **11** (2019) 1000. https://doi.org/10.3390/rs11091000

21　J. Hong, A. Kong, J. Liang, and C. Chen: Int. Conf. Geogr. Inf. Remote Sens. Technol. (GIRST 2022) 911–916. https://doi.org/10.1117/12.2667750

22　M. Guo, M. Sun, D. Pan, G. Wang, Y. Zhou, B. Yan, and Z. Fu: Heritage Sci. **11** (2023) 1. https://doi.org/10.1186/s40494-022-00833-z

23　W. Sulzer, J. Gspurning, V. Kaufmann, R. Fuerhacker, J. Catau, F. Wack, and D. Held: J. Mediterr. Cities. **3** (2023) 1. https://doi.org/10.38027/mediterranean-cities_vol3no1_1

24　Y. Liu, C. Zhao, Q. Zhang, and W. Zhu: JGG. **37** (2017) 787. http://www.jgg09.com/EN/Y2017/V37/I8/787

About the Authors

Guo Ming, a professor and Ph.D. supervisor of Han descent from Hubei Huangpi, graduated from Wuhan University's State Key Laboratory of Remote Sensing Information Engineering in 2011 and holds a Ph.D. degree in engineering. He also serves as a reviewer for the Chinese National Natural Science Foundation and renowned domestic and international SCI journals, including Automation in Construction. He focuses primarily on 3D GIS research and LIDAR technology use. His research interests include building health monitoring, LiDAR mapping technology, and the digital preservation of cultural assets. (guoming@bucea.edu.cn)

Wei Yaxuan is a graduate student at the Architectural Heritage Digitization Lab, part of the School of Geomatics and Urban Spatial Informatics at Beijing University of Engineering and Architecture. Her research focuses on InSAR (interferometric synthetic aperture radar) settlement monitoring. (2670404838@qq.com)

Chen Zhaorui completed her undergraduate studies at Beijing University of Architecture, with a research focus on geospatial information. She is currently a graduate student at Lingnan University in Hong Kong, where her research is focused on urban governance, specifically in the area of sustainable development. (2252557559@qq.com)

Zhao Youshan is from Nanyang, Henan, and works at the China Academy of Building Research Co., Ltd. He earned his master's degree in cartography and geographic information engineering from Beijing University of Engineering and Architecture in 2008. His primary field of work is structural inspection. (yshzhao@163.com)

Tang Xingyu is a graduate student in the Architectural Heritage Digitization Lab, part of the School of Geomatics and Urban Spatial Informatics at Beijing University of Engineering and Architecture. Her research focuses on simultaneous localization and mapping (SLAM).

Guo Kecai from Wuhan, Hubei, is a senior engineer. He graduated from Ezhou University in 2006. He is currently the general manager of Beijing Shenxindacheng Technology Co., Ltd., and is mainly engaged in research on mobile LiDAR scanning, engineering measurement, and automation technology. (1033547194@qq.com)

Tang Kun is a member of the Communist Party of China and a senior engineer with a master's degree in structural engineering from Beijing Jiaotong University. He currently serves as the Deputy Dean of the Second Inspection Institute and is an emergency assessment expert for building structures at the Beijing Safety Appraisal Industry Association. He has long been engaged in the inspection and identification of building structures, performance evaluation, and engineering accident analysis. He has been the chief editor or co-editor of four standards and specifications, holds two invention patents, and has participated in the 'Fourteenth Five-Year Plan' project. (13810644286@126.com)